- RESEARCH PAPER -

International Journal of Mining and Geo-Engineering

IJMGE

IJMGE 55-1 (2021) 1-6

DOI: 10.22059/ijmge.2020.292606.594832

Application of Artificial Neural Network for Stability Analysis of Undercut Slopes

Hassan Sarfaraz [a], Mohammad Hossein Khosravi [a,*], Thirapong Pipatpongsa [b], Hassan Bakhshandeh Amnieh [a]

[a] *School of Mining Engineering, College of Engineering, University of Tehran, Iran*

[b] *Department of Urban Management, Kyoto University, Japan*

Article History:

Received: 16 November 2019,

Revised: 17 May 2020,

Accepted: 06 June 2020.

ABSTRACT

One of the significant tasks in undercut slopes is determining the maximum stable undercut span. According to the arching effect theory, undercut excavations cause the weight of the slope to be transmitted to the adjacent stable regions of the slope, which will increase the stability of the slope. In this research, determining the maximum width of undercut slopes was examined through numerical modeling in the FLAC3D software. For this purpose, a series of undercut slope numerical models, with various slope angles, horizontal acceleration coefficients, and counterweight balance widths was conducted, and the results were validated using the corresponding experimental test results. The effect of each parameter on the maximum stable undercut span was investigated with an artificial neural network, where a multi-layer perceptron (MLP) model was performed. The results showed good accuracy of the proposed MLP model in the prediction of the maximum stable undercut span. In addition, a sensitivity analysis demonstrated that the dip angle and horizontal acceleration coefficient were the most and least effective input variables on the maximum stable undercut span, respectively.

Keywords : *Undercut Slope; Numerical Modeling; Artificial Neural Network; Multi-layer Perceptron Model*

1. Introduction

The arching effect is a significant phenomenon in geo-materials, in which loads tend to transfer from a yielding portion of the media to adjacent stationary portions, leading to the redistribution of stress [1]. Janssen [2] investigated the development of arching in granular silos in 1895. He illustrated that the applied horizontal pressure to a silo wall would increase nonlinearly with increasing the depth and developed the theory of arching. In 1943, the formation of arches in geo-materials was investigated by Terzaghi [3] through a series of physical models. Later, this phenomenon was investigated in various geotechnical engineering problems, such as retaining walls, underground spaces, slopes, and so on. In 1986, Bosscher and Gray [4] examined the arching effect in slopes by carrying out some experimental tests.

The word *undercut slopes* refers to such a slope in whose front portion the excavation process is performed. Determining the maximum stable undercut span is an important issue. This span depends on various parameters, such as strength parameters of soil and the geometry of the slope [5]. Pipatpongsa et al. [6], based on the arching effect, suggested a procedure for the mining processes in the Mae-Moh open-pit mine, as a technique in increasing the stability of undercut slopes without reinforcement. Following this technique, Khosravi et al. [7] studied the arching effect in undercut slopes by conducting a series of physical modelings. They carried out experimental undercut slope tests under 1g and centrifugal conditions. The results of their study indicated that a fraction of yielded soil weight would be transferred to the adjacent stable portions through the undercut process [8, 9]. They proposed that, for stabilizing undercut slopes, the counterweight balance method can be used as a new technique [10,11]. Recently, Khosravi et al. [12] performed a series of undercut slope centrifugal modelings and demonstrated that the arching phenomenon could occur even at higher stress levels. Ouch et al. [13] conducted numerical modeling on a soil block on a plane with low friction in two types of with and without side supports. They examined the influence of slope width and thickness as well as the number and position of shear pins on slope stability using experimental and numerical models [14-18].

In this research, the influence of slope angle, horizontal acceleration coefficient, and counterweight balance width was studied through a series of numerical modelings under pseudo-static loading. In the stability analysis under pseudo-static conditions, dynamic loads are replaced with static forces with components in both horizontal and vertical directions. Since the vertical component has a negligible impact on the stability of slopes, it was not considered in such an analysis [19]. In addition, the artificial neural network (ANN) was used in the interpretation of numerical simulations, and the results were discussed.

2. Implication of an artificial neural network

An artificial neural network (ANN) consists of many data processing units named neurons. The network is skillful for simulating the performance of the human brain structure based on the trial and error method using neurons [20]. In an ANN model, the neurons are connected to each other. Generally, a neural network model is usually composed of at least three layers: an input layer, hidden layers, and an output layer. The schematic view of a typical neural network is presented in Fig. 1 [21].

* Corresponding author. Tel.: +98-2182084398, Fax: +98-2188008838, *E-mail address:* mh.khosravi@ut.ac.ir (M.H. Khosravi).

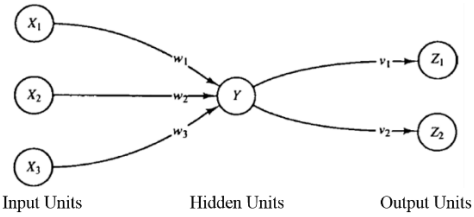

Fig. 1- Schematic view of a typical neural network [21].

In an ANN model, the major calculation process is performed in the hidden layers. Neurons in every layer are linked to neurons in the adjacent layer with a coefficient called weight (w). The transform function is used to transform the weighted summation of the input signal near a neuron and for calculating the output response of neurons. Two useful non-linear sigmoid transform functions are TANSIG and LOGSIG, which are commonly used in the neural network [22]. According to Fig. 1, the output of the input layer is used as an input signal for the hidden layers. The optimal number of neurons and hidden layers and also the amount of goal error are calculated based on the rule of trial and error [23]. In the first step, the artificial neural network is trained by a portion of the input data. Then, the network is verified by the portion of the input data. In the training procedure, the input signal is entered, and the output value is determined. Consequently, the error between the actual and predicted values can be calculated. According to this error, the weight is adjusted by starting from the output layer to the input layer. This technique is known as the algorithm of back-propagation and is useful for executing the prediction model [21]. The multi-layer perceptron (MLP) was proposed by Rumelhart [24]. Usually, in this model, the input layer normalizes the input values. This type of data preparation and normalization improves network performance. This method of data normalization has been utilized by many researchers [25-28].

3. A review of physical modeling

In this study, a numerical investigation was established to complete the results of the pre-conducted physical modeling study [10]. The geometry of the physical model is illustrated in Fig. 2.

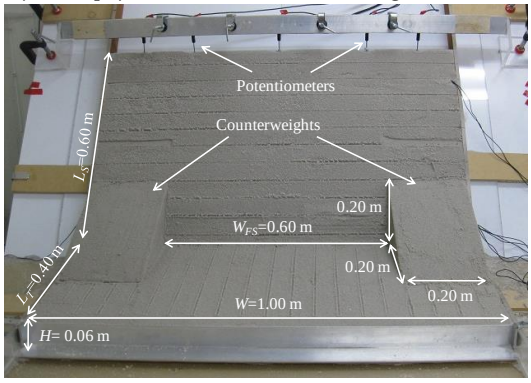

Fig. 2- Geometry of the physical model [10].

The material properties of experimental tests are listed in Table 1. The values of cohesion measured by physical models range from 0.36 kPa to 0.8 kPa for the used modeling material. The reason was that the cohesion was the most varied parameter due to uncertainties of the suction effect in the moist sand of the experimental model. Leelasukseree et al. [29] obtained an appropriate cohesion value of 0.8 kPa by comparing the numerical model results with those of the corresponding physical model.

4. Numerical modeling

FLAC3D, which is based on the Lagrangian formulation and is appropriate for large deformation analysis, was used for numerical modeling in this study [30]. A schematic view of the numerical model is presented in Fig 3. The geometry of the numerical models kept exactly similar to that of physical models shown in Fig. **2**.

Table 1- Material properties of physical modeling [10,29].

Density	1395 kg/m³
Specific density	2.65
Elastic modulus	4 Mpa
Poisson's ratio	0.25
Maximum void ratio	1.132
Minimum void ratio	0.711
Water content	10 %
Normal interface stiffness	1 GPa/m
Shear interface stiffness	1 GPa/m
Internal friction angle	41.5°
Interface friction angle	18.5°
Cohesion	0.8 kPa
Adhesion	0.1 kPa

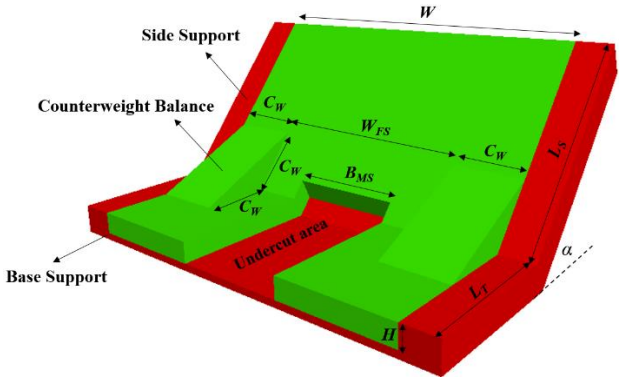

Fig 3- A schematic view of the numerical model.

The model was made of cubic elements with a size of 2 cm. The model consisted of two portions: the base portion with the sizes of W=100 cm and L_T=40 cm and the slope portion with the sizes of W=100 cm and L_S=60 cm. The thickness of the model was H=6 cm in both base and slope portions. In Fig 3, C_w denotes a counterweight balance width. The soil was considered as a Mohr-Coulomb material, and the constitutive criteria for base and side supports were linear elastic. The properties of the soil, measured in physical models (Table 1), were also used in numerical models. For each slope angle, the front central portion was excavated in the subsequent steps with a width of 4 cm. In each step of excavation, the width of the cut section was symmetrically increased toward the left and right sides of the model. After each step, the numerical model was performed, and the unbalanced force was calculated. When the force approached zero, the numerical model reached a stable condition, followed by the subsequent step of excavation. If the unbalanced force did not approach zero, the slope was considered unstable, and the maximum width of undercut (B_f) was recorded. The numerically computed values for the width of the undercut span for different slope angles (α equal to 40º to 75º) in the static and pseudo-static conditions, with horizontal acceleration coefficients of K_h = 0, 0.1, 0.2, and 0.3, and counterweight widths of C_w = 0, 10, 20, and 30 cm, are presented in Table 2. Note that, considering the total width of 1 m for the model, in slope dip angles (α) of 40 and 45 degrees, the maximum stable undercut span in the absence of counterweight balance (C_w=0) was bigger than 40 cm. Hence, the counterweight balance with a width of 30 cm was not applicable.

In Table 3, the numerical results under static conditions (K_h = 0) were compared with the results of physical models [10]. The good agreement between the results of numerical and physical models validated the simulation conducted in this study.

The influences of slope dip angle (α), counterweight width (C_w), the horizontal acceleration coefficient (K_h), and the normalized free span (W_{FS}/W) on the maximum normalized stable undercut span (B_{MS}/W_{FS})

are shown in Table 4 and Fig 4. The free span is defined as the span between two counterweights ($W_{FS}=W-2C_w$), as indicated in Fig 3.

Table 2- The results of the numerical model in terms of the maximum stable undercut span (B_{MS}: cm).

Angle of slope (α: degree)	Width of counterweight (C_w: cm)	K_h 0	0.1	0.2	0.3
40	0	52	36	0.2	24
	10	56	36	28	24
	20	60	36	28	28
45	0	40	32	32	24
	10	40	32	28	24
	20	44	32	28	24
50	0	32	28	28	24
	10	32	28	24	24
	20	36	28	24	24
	30	40	32	24	24
55	0	28	24	28	20
	10	28	24	24	20
	20	32	24	24	20
	30	36	28	24	24
60	0	24	24	24	20
	10	24	24	20	20
	20	24	24	20	20
	30	28	28	20	24
65	0	24	20	24	20
	10	24	20	20	20
	20	24	20	20	20
	30	24	24	20	20
70	0	20	20	20	16
	10	20	20	20	16
	20	20	20	20	16
	30	20	20	20	20
75	0	20	20	20	4
	10	20	20	16	4
	20	20	20	16	4
	30	20	20	16	4

Table 3- Comparison of the numerical and physical results under the static condition (K_h=0).

Angle of slope (α: degree)	Width of counterweight (C_w: cm)	Maximum stable undercut span (B_{MS}: cm) Physical models [10]	Numerical models
40	0	50	52
50	0	35	32
	20	40	36
	30	45	40
60	0	25	24
70	0	20	20

Table 4- Maximum normalized stable undercut span (B_{MS}/W_{FS}).

Angle of slope (α: degree)	Horizontal acceleration coefficient (K_h)	Normalized free span (W_{FS}/W) 1 (C_w=0 cm)	0.8 (C_w=10 cm)	0.6 (C_w=20 cm)	0.4 (C_w=30 cm)
40	0	0.52	0.7	1	---
	0.1	0.36	0.45	0.6	---
	0.2	0.28	0.35	0.533	---
	0.3	0.24	0.3	0.467	---
45	0	0.4	0.5	0.733	---
	0.1	0.32	0.4	0.533	---
	0.2	0.28	0.35	0.467	---
	0.3	0.24	0.3	0.4	---
50	0	0.32	0.4	0.6	1
	0.1	0.28	0.35	0.467	0.8
	0.2	0.24	0.3	0.4	0.7
	0.3	0.24	0.3	0.4	0.6
55	0	0.28	0.35	0.533	0.9
	0.1	0.24	0.3	0.4	0.7
	0.2	0.24	0.3	0.4	0.6
	0.3	0.2	0.25	0.333	0.6
60	0	0.24	0.3	0.4	0.7
	0.1	0.24	0.3	0.4	0.7
	0.2	0.2	0.25	0.333	0.6
	0.3	0.2	0.25	0.333	0.6
65	0	0.24	0.3	0.4	0.6
	0.1	0.2	0.25	0.333	0.6
	0.2	0.2	0.25	0.333	0.5
	0.3	0.2	0.25	0.333	0.5
70	0	0.2	0.25	0.333	0.5
	0.1	0.2	0.25	0.333	0.5
	0.2	0.2	0.25	0.333	0.5
	0.3	0.16	0.2	0.267	0.5
75	0	0.2	0.25	0.333	0.5
	0.1	0.2	0.25	0.333	0.5
	0.2	0.16	0.2	0.267	0.5
	0.3	0.04	0.05	0.067	0.1

According to Fig 4, regardless of the slope angle, increasing the width of the counterweight, and therefore decreasing the free span made the slope more stable, leading to a wider undercut span. These results are in agreement with the results of physical models [10], confirming the application of counterweight balance as a useful method in stabilizing the undercut slopes. However, it is noticeable that the influence of counterweight balance is ignorable at slope angles of greater than 60 degrees.

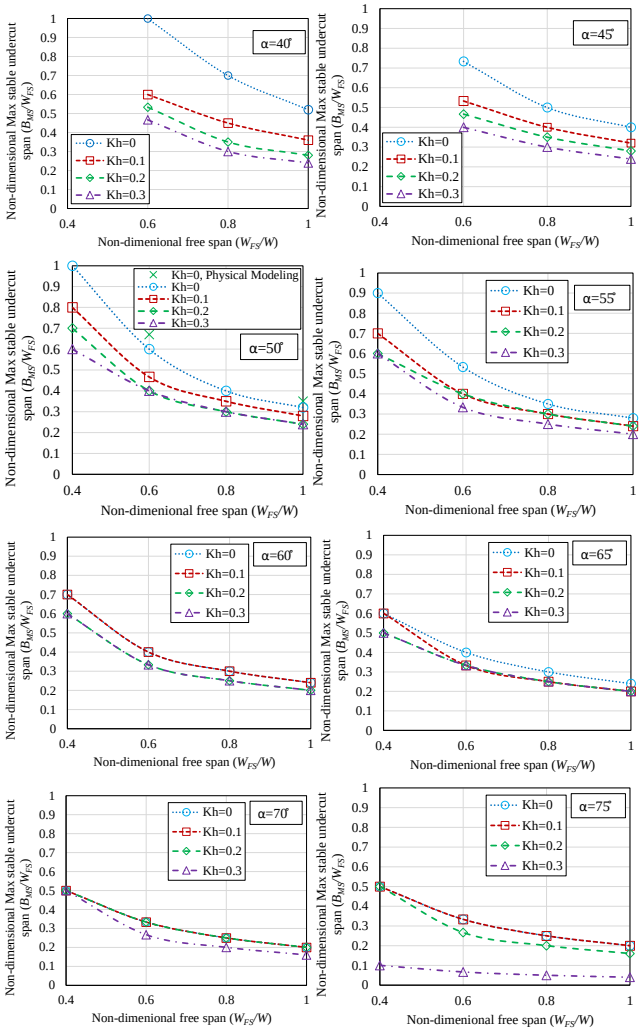

Fig 4- Numerical results revealing maximum undercut span versus free span.

The contour of failure modes in the numerical model with α=50°, K_h=0, and Cw=0 cm, is shown in Fig. 5. As this figure shows, the shear cracks initiate from the corners of the undercut area, while other regions are under the tensile stress. The symbols *p* and *n* in the legend of this figure represent the model state in the previous and the current steps, respectively.

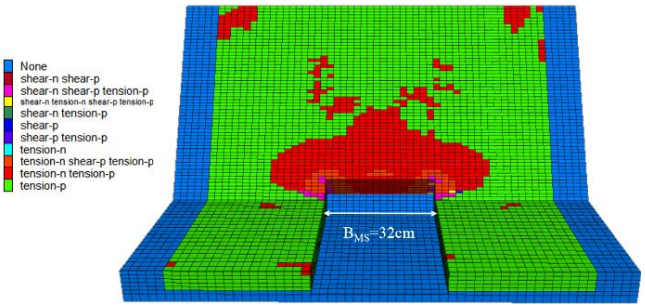

Fig. 5- The contour of the failure mode in the model test with α=50º, K_h=0 and Cw=0 cm.

5. Application of ANN

5.1. Data normalization

The raw data obtained from the numerical model should be normalized to increase the processing and convergence rate of the ANN during the training process and to minimize the prediction error [22]. By normalizing the data, their value will be in the range of 0 to 1. The relation of normalization based on unity is presented in Equation 1 [31].

$$A_{Norm} = \frac{A - A_{min}}{A_{max} - A_{min}} \quad (1)$$

Where:

A is any raw data

A_{min} is the minimum value of data

A_{max} is the maximum value of data

A_{Norm} is the normalized data

5.2. Designing the optimum architecture of the MLP model

The data attained from the numerical simulation (Table 4) were used to prepare the MLP model for prediction purposes. In this research, all of the data were separated into three parts: training data (70 percent of total data), testing data (15 percent of total data), and validation data (15 percent of total data). The optimized architecture of the MLP model, such as the number of hidden layers and the number of neurons in the hidden layer, can be computed based on the trial and error rule [28]. The optimum number of neurons is determined based on the root mean squared error (*RMSE*) value. For this purpose, different varieties of neurons are embedded in the hidden layers of the model, and their corresponding *RMSE* value is calculated according to equation 2. Network performance for a different number of neurons in the hidden layer is shown in Fig. 6. According to this figure, the minimum value of *RMSE* is achieved by eight neurons.

$$RMSE = \sqrt{\frac{1}{N}\sum_{i=1}^{N}\left(\overline{A_i} - A_i\right)^2} \quad (2)$$

Where:

RMSE: Root Mean Squared Error

$\overline{A_i}$: ith predicted value of the target

A_i : ith measured value of the target

N: number of datasets

Therefore, eight neurons should be arranged in one or two hidden layers. In theory, only one hidden layer is sufficient for networks with a back-propagation algorithm. According to Flood and Kartam [25], the MLP model with a minimum of 2 hidden layers offer more flexibility to model complex problems. In this way, a different arrangement of eight neurons is considered in two hidden layers. The training function of trainlm Levenberg-Marquardt was considered in this study. Moreover, the value of the learning rate was selected as the default value in the MATLAB software. The results of RMSE values based on two transform functions of TANSIG (tangential non-linear sigmoid) and LOGSIG (logarithmic non-linear sigmoid) are illustrated in Table 5. According to the Table, the 3-[6-2]-1 neuron arrangement had the highest efficiency due to its minimum *RSME* value. The optimized architecture of the MLP model is presented in Fig. 7.

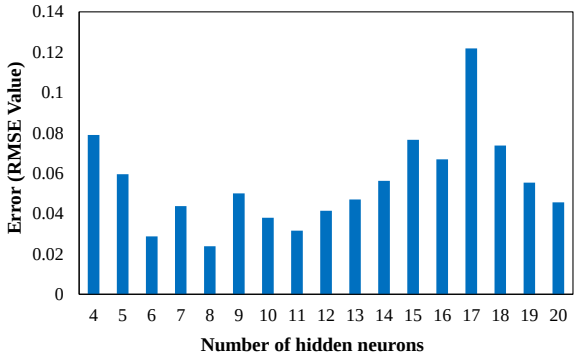

Fig. 6- Network performance for a different number of neurons in the hidden layer.

Table 5- The optimum arrangement of neurons in two hidden layers.

No.	Network Arrangement	*RMSE* Error Transfer Function: TANSIG	*RMSE* Error Transfer Function: LOGSIG
1	3-[8]-1	0.0282	0.0279
2	3-[1-7]-1	0.0511	0.0387
3	3-[2-6]-1	0.0265	0.0323
4	3-[3-5]-1	0.0274	0.0415
5	3-[4-4]-1	0.0342	0.0413
6	3-[5-3]-1	0.0433	0.0259
7	3-[6-2]-1	0.0256	0.0193
8	3-[7-1]-1	0.0393	0.0666

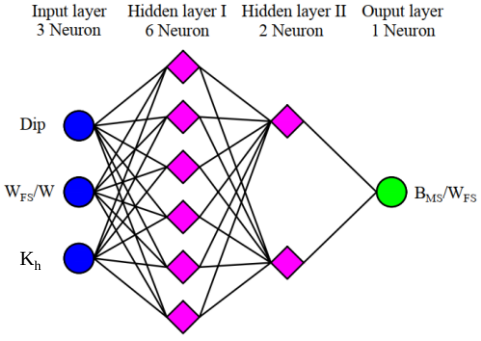

Fig. 7- The optimized architecture of the MLP Model.

5.3. Evaluating the performance of the model

The performance of the MLP model should be evaluated in predicting the capability of output. Hence, four performance indices of correlation coefficient (R^2), the variance accounted for (*VAF*), coefficient of efficiency (*CE*), and root mean squared error (*RMSE*) are employed and computed using the testing dataset. These datasets are chosen randomly from the database and are not contained within the training phase. R^2, *VAF*, and *CE* values are calculated using Equations 3 to 5.

$$R^2 = \left| \frac{\sum_{i=1}^{N}\left(\overline{A_i} - \overline{A_{avg}}\right)\left(A_i - A_{avg}\right)}{\sqrt{\sum_{i=1}^{N}\left(\overline{A_i} - \overline{A_{avg}}\right)^2 \sum_{i=1}^{N}\left(A_i - A_{avg}\right)^2}} \right|^2 \quad (3)$$

$$VAF = 100\left(1 - \frac{Var\left(A_i - \overline{A_i}\right)}{Var\left(A_i\right)}\right) \quad (4)$$

$$CE = 1 - \frac{\sum_{i=1}^{N}\left(\overline{A_i} - A_i\right)^2}{\sum_{i=1}^{N}\left(\overline{A_i} - \overline{A_{avg}}\right)} \quad (5)$$

In which:

$\overline{A_i}$: ith predicted value

A_i : ith measured value

A_{avg} : The average of measured values

$\overline{A_{avg}}$: The average of predicted values

Var: variance

N: number of datasets

The lower the *RMSE*, the higher the efficiency of the network [26]. In an ideal state, the value of *RMSE* and *CE* are zero and one, respectively. The *VAF* parameter defines the degree of difference between the variances of predicted and measured data. The *VAF* value was almost 100%, which demonstrated low variability. The indices mentioned above are presented in Table 6.

Table 6- Performance indices of the MLP model.

RMSE	R^2 (%)	*VAF* (%)	*CE*
0.0263	99.99	99.90	98.03

The graphs of correlation coefficients for training, test, validation, and the whole set of data are illustrated in Fig. 8. According to this figure, the maximum values of *R* for training, validation, test, and the whole set of data are obtained 0.993, 0.995, 0.986, and 0.992, respectively, which indicates high conformity between predicted and measured values. Also, the rate of changes in the error level during the iterations is shown in Fig. 9. As seen, by using the magnifying MSE curve when training the model, the best validation performance obtained at epoch 18, and the value of MSE was 0.0011, showing the excellent performance of the model.

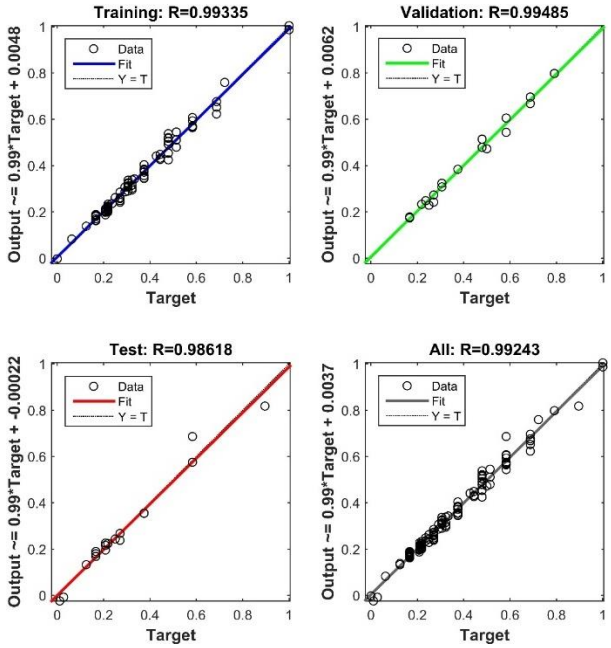

Fig. 8- Correlation coefficient of the output parameter.

5.4. Sensitivity analysis

Sensitivity analysis is a procedure by which the effect of each input variable on the output parameter is described. One of the sensitivity analysis methods is Cosine Amplitude Method (*CAM*) [27]. Data array (*X*) is defined as:

$$X = \{X_1, X_2, X_3, X_4, ..., X_n\} \quad (6)$$

In data array *X*, every component x_i is a vector with *k* dimension:

$$X_i = \{x_{i1}, x_{i2}, x_{i3}, x_{i4}, ..., x_{ik}\} \quad (7)$$

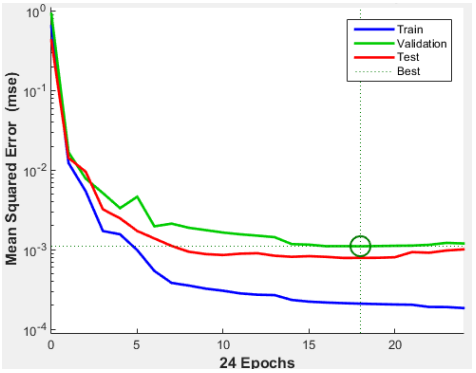

Fig. 9- The best validation performance of the model during the training.

Therefore, all data can be considered, such as a point in the *k* dimensional space, where every point has *k* coordinates for a full delineation. Therefore, the strength relation (r_{ij}) between the data pairs of x_i, and x_j is given in Equation 8:

$$r_{ij} = \frac{\left|\sum_{m=1}^{k} x_{im} x_{jm}\right|}{\sqrt{\left(\sum_{m=1}^{k} x_{im}^2\right)\left(\sum_{m=1}^{k} x_{jm}^2\right)}} \quad (8)$$

By applying Equation 8, strength value relation (r_{ij}) between the input parameters (*Dip*, W_{FS}/W and K_h) and output parameter is shown in Fig. 10. As indicated in this figure, the most efficient parameter on the output is the dip angle, while K_h has the minimum effect on the output.

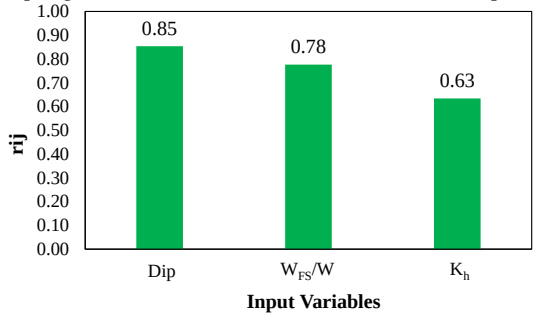

Fig. 10- Strength value relation (r_{ij}) between input and output parameters.

6. Conclusion

In this research, the maximum undercut span was modeled using the finite difference software (FLAC 3D) under pseudo-static conditions. The results of numerical modelings showed that the influence of counterweight balance in mild slopes was more than the steep slopes so that in slopes steeper than 60 degrees, the counterweight balance had no significant influence on increasing the stability under both static and pseudo-static conditions. For steep slopes, the maximum width of undercut does not differ under both static and pseudo-static conditions. Additionally, under static conditions, as the angle of the slope increased, the maximum width of undercut decreased. Moreover, by increasing the horizontal acceleration coefficient, the maximum width of undercut decreased at a low rate. The results of numerical modeling were evaluated by an artificial neural network. It was seen that in the 3-[6-2]-1 architecture of neurons, the values of *RMSE* were 0.0256 and 0.0193 for TANSIG and LOGSIG transfer functions, respectively. The

performance of the proposed MLP model was assessed using the R^2, *RMSE*, *VAF*, and *CE* indices. The results demonstrated that the proposed MLP model had high conformity with the real measured data. Finally, the sensitivity analysis was conducted for evaluating the influence of each input variable on the output parameter. It was concluded that the slope dip angle and the horizontal acceleration coefficient (K_h) had maximum and minimum effects on the maximum stable span of the undercut, respectively.

REFERENCES

[1] R. L. Handy, "The Arch in Soil Arching," *J. Geotech. Eng.*, vol. 111, no. 3, pp. 302–318, Mar. 1985.

[2] H. A. Janssen, "Versuche uber getreidedruck in Silozellen," *Zeitschrift des Vereins Dtsch. Ingenieure*, no. 35, pp. 1045–1049, 1895.

[3] K. Terzaghi, "Theoretical soil mechanics. John Wiley & Sons, New York.," *Theor. soil Mech. John Wiley Sons, New York.*, 1943.

[4] P. J. Bosscher and D. H. Gray, "Soil Arching in Sandy Slopes," *J. Geotech. Eng.*, vol. 112, no. 6, pp. 626–645, 1986.

[5] M. Khosravi, "Arching effect in geomaterials with applications to retaining walls and undercut slopes," PhD. Dissertation, Tokyo Institute of Technology, 2012.

[6] T. Pipatpongsa, M. H. Khosravi, P. Doncommul, and N. Mavong, "Excavation problems in Mae Moh lignite open-pit mine of Thailand," in *Proceedings of Geo-Kanto2009*, 2009, vol. 12, pp. 459–464.

[7] M. H. Khosravi, T. Pipatpongsa, C. Leelasukseree, and P. Wattanachai, "Failure mechanisms in arched excavation of sloped earth using model test," *Proc. Geo-Kanto2009*, vol. 12, pp. 241–246, 2009.

[8] M. H. Khosravi, Y. Ishii, J. Takemura, and T. Pipatpongsa, "Centrifuge model test on compacted sand slopes undercut by in-flight excavator," *Proc. Geo-Kanto2010*, pp. 4–5, 2010.

[9] M. Khosravi, T. Pipatpongsa, A. Takahashi, and J. Takemura, "Arch action over an excavated pit on a stable scarp investigated by physical model tests," *Soils Found.*, vol. 51, no. 4, pp. 723–735, 2011.

[10] M. Khosravi, L. Tang, T. Pipatpongsa, J. Takemura, and P. Doncommul, "Performance of counterweight balance on stability of undercut slope evaluated by physical modeling," *Int. J. Geotech. Eng.*, vol. 6, no. 2, pp. 193–205, Apr. 2012.

[11] M. Khosravi, H. Sarfaraz, M. Esmailvand, and T. Pipatpongsa, "A Numerical Analysis on the Performance of Counterweight Balance on the Stability of Undercut Slopes," *Int. J. Min. Geo-Engineering*, vol. 51, no. 1, pp. 63–69, 2017.

[12] M. H. Khosravi, J. Takemura, T. Pipatpongsa, and M. Amini, "In-flight excavation of slopes with potential failure planes," *J. Geotech. Geoenvironmental Eng.*, vol. 142, no. 5, p. 6016001, 2016.

[13] R. Ouch, B. Ukritchon, and T. Pipatpongsa, "Stability of soil block on low interface friction plane with and without side supports," *Eng. J.*, vol. 20, no. 2, pp. 123–145, 2016.

[14] R. Ouch, B. Ukritchon, T. Pipatpongsa, and M. H. Khosravi, "Experimental investigations of shear pin arrangement on soil slope resting on low interface friction plane," *Maejo Int. J. Sci. Technol.*, vol. 10, no. 3, pp. 313–329, 2016.

[15] R. Ouch, B. Ukritchon, T. Pipatpongsa, and M. H. Khosravi, "Finite element analyses of the stability of a soil block reinforced by shear pins," *Geomech. Eng.*, vol. 12, no. 6, pp. 1021–1046, 2017.

[16] B. Ukritchon, R. Ouch, T. Pipatpongsa, and M. H. Khosravi, "Investigation of stability and failure mechanism of undercut slopes by three-dimensional finite element analysis," *KSCE J. Civ. Eng.*, vol. 22, no. 5, pp. 1730–1741, 2018.

[17] B. Ukritchon, R. Ouch, T. Pipatpongsa, and M. H. Khosravi, "Experimental studies of floor slip tests on soil blocks reinforced by brittle shear pins," *Int. J. Geotech. Eng.*, vol. 13, no. 1, pp. 1–8, 2019.

[18] B. Ukritchon, R. Ouch, T. Pipatpongsa, and M. H. Khosravi, "Physical and numerical studies of stability of soil blocks reinforced by brittle shear pins," *Acta Geotech.*, vol. 14, no. 6, pp. 2103–2122, 2019.

[19] S. L. Kramer, *Geotechnical earthquake engineering. In prentice--Hall international series in civil engineering and engineering mechanics*. 1996.

[20] D. E. Rumelhart, G. E. Hinton, and R. J. Williams, "Learning representations by back-propagating errors," *Nature*, vol. 323, no. 6088, pp. 533–536, 1986.

[21] L. V Fausett and others, *Fundamentals of neural networks: architectures, algorithms, and applications*, vol. 3. Prentice-Hall Englewood Cliffs, 1994.

[22] R. Rojas, *Neural networks: a systematic introduction*. Springer Science & Business Media, 2013.

[23] A. Majdi and M. Rezaei, "Application of Artificial Neural Networks for Predicting the Height of Destressed Zone Above the Mined Panel in Longwall Coal Mining," *47th US Rock Mech. Symp.*, 2013.

[24] F. Rosenblatt, "The perceptron: A probabilistic model for information storage and organization in the brain," *Psychol. Rev.*, vol. 65, no. 6, pp. 386–408, 1958.

[25] I. Flood and N. Kartam, "Neural Networks in Civil Engineering. I: Principles and Understanding," *J. Comput. Civ. Eng.*, vol. 8, no. 2, pp. 131–148, Apr. 1994.

[26] M. H. Den Hartog, R. Babuška, H. J. R. Deketh, M. Alvarez Grima, P. N. W. Verhoef, and H. B. Verbruggen, "Knowledge-based fuzzy model for performance prediction of a rock-cutting trencher," *Int. J. Approx. Reason.*, vol. 16, no. 1, pp. 43–66, 1997.

[27] T. J. Ross, *Fuzzy Logic With Engineering. Second Edition*. 2004.

[28] A. Rastbood, Y. Gholipour, and A. Majdi, "Stress Analysis of Segmental Tunnel Lining Using Artificial Neural Network," *Period. Polytech. Civ. Eng.*, vol. 61, no. 4, pp. 664–676, 2017.

[29] C. Leelasukseree, T. Pipatpongsa, M. H. Khosravi, N. Mavong, and others, "Stresses and a failure mode from physical and numerical models of undercut slope lying on inclined bedding plane," in *ISRM Regional Symposium-7th Asian Rock Mechanics Symposium*, 2012.

[30] I. G. Inc, *"FLAC3D Fast Lagrangian Analysis of Continua in 3 Dimension*. 2015.

[31] B. Etzkorn, "Data normalization and standardization," *BE BLOG [Online]. Available http//www. benetzkorn. com/2011/11/data-normalization-and-standardization*, 2011.